Carbonates at high pressures: Possible carriers for deep carbon reservoirs in the Earth's lower mantle

M. L. Marcondes,[1,*] J. F. Justo,[2,*] and L. V. C. Assali[1]
[1]*Instituto de Física, Universidade de São Paulo, CEP 05508-090, São Paulo, SP, Brazil*
[2]*Escola Politécnica, Universidade de São Paulo, CP 61548, CEP 05424-970, São Paulo, SP, Brazil*
(Received 13 June 2016; published 23 September 2016)

The high-pressure structural and elastic properties of $MgCO_3$, $CaCO_3$, and $MgCa(CO_3)_2$ have been investigated with density functional theory. By computing the isotropic elastic constants, we found that the bulk and shear acoustic wave velocities are smaller in carbonates than in their respective silicates for a wide range of pressure. In terms of geophysics, these results provide strong evidence that the low-velocity zones, near the bottom of the Earth's lower mantle, could be associated with the presence of carbon element in the form of carbonate minerals. This is a different model, associated with chemical differentiation, to explain those low-velocity zones, in addition to several other recent ones proposed in the literature.

DOI: 10.1103/PhysRevB.94.104112

I. INTRODUCTION

Carbon is a unique chemical element, present in a large number of systems, which plays a major role in many fields, such as chemistry, biology, physics, and geophysics [1]. Within a fundamental point of view, the widespread interest in this element stems from the rich chemical nature of its interatomic interactions, particularly the possibility of getting stable structures in several hybridizations and microscopic configurations. Carbon could be found in nature in a number of structures, such as diamond, graphite, polymers, fullerenes, and diamondoids, as well as many others. Specifically, the development of high pressure-high temperature processes to grow synthetic diamond has paved the way for intensive research in those extreme thermodynamic conditions [2].

Over the last few years, carbon has attracted great interest in geophysics and, consequently, in other celestial bodies [3]. Carbon is present in mild concentrations on the Earth's surface, being a crucial chemical element for life. Considering the current knowledge of the chemical composition of the solar system, based on data from meteorites that have hit the Earth, it has been established the amount of carbon that should be present on the Earth. Since carbon is the fourth most abundant element in the solar system, the major conclusion is that a considerable amount of carbon is missing on the Earth's crust, and it should be stored on its mantle or core [4]. This conclusion is substantiated by results that showed the presence of CO_2 in magmas [5,6] and mantle mineral inclusions in natural diamonds [7].

Within a geophysics perspective, there is an extensive list of open questions on deep carbon that remain to be addressed [3]. One of the greatest challenges is to understand the carbon cycle on the Earth, i.e., the transport of carbon from surface to deep interior and vice versa. In order to build a more precise compositional model of the Earth's interior, it is important to determine the amount of carbon stored in the mantle and core, as how it is stored there, segregated or dissociated within major mantle minerals [3]. Since carbon solubility is low in silicates ($MgSiO_3$ and $CaSiO_3$), carbon could be stored in the form of carbonates, such as $MgCO_3$ and $CaCO_3$.

Many of those questions could be addressed by exploring the properties of the Earth's minerals and their alloys, by experiments with high pressure-high temperature measurements or by theory with self-consistent thermodynamic models combined with atomistic simulations. This theoretical framework may provide elements to improve knowledge of properties of minerals at high pressures and high temperatures, such as the properties of carbon at those thermodynamic conditions [1]. Quantum mechanics atomistic simulations represent a powerful tool to inspect the physical properties of materials [8,9]. Notably in geophysics, such methodologies have been extensively used to study a number of mineral systems [10].

Here, we performed a first principles investigation on the structural and elastic properties of magnesium ($MgCO_3$), calcium ($CaCO_3$), and magnesium-calcium [$MgCa(CO_3)_2$] carbonates at high pressures. Although the structural properties of those minerals have been explored by some theoretical investigations [11–13], the literature lacks broader researches on their elasticity, which is crucial to understand the role of carbon on mantle properties. This paper is organized as follows. Section II presents the theoretical model. Sections III, IV, and V present, respectively, the properties of $MgCO_3$, $CaCO_3$, and $MgCa(CO_3)_2$ and the geophysical implications of those results.

II. METHODOLOGY

The calculations were performed using the Quantum ESPRESSO computational package [9]. The electronic interactions were described within the density functional theory, considering the exchange-correlation potential based on the LDA (local density approximation) [14] or the GGA (generalized gradient approximation) [15] functionals. The electronic wave functions were expanded using the PAW (projected augmented wave) method [16], with a plane wave cutoff of 90 Ry. Brillouin zones for electronic states were sampled by a displaced $4\times4\times4$ **k** mesh. For each pressure, from -15 to 150 GPa, the structures were optimized using the damped variable cell shape molecular dynamics method [17,18]. Then, a second order Birch-Murnaghan equation of state was used to fit the compression data.

In order to calculate the elastic coefficients (C_{ijkl}) of each mineral at a certain pressure P, negative and positive strains

*michel@if.usp.br; jjusto@lme.usp.br

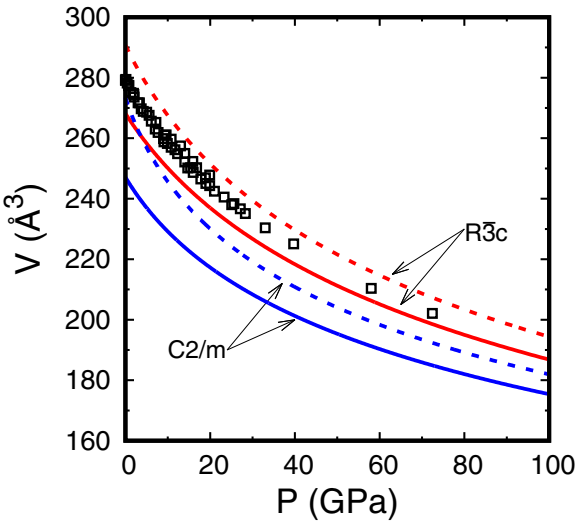

FIG. 1. Equation of state of $MgCO_3$ in the $R\bar{3}c$ (red lines) and $C2/m$ (blue lines) phases, computed with the LDA (full lines) and GGA (dashed lines) functionals. Experimental data (□) are from Ref. [21].

of 1% were applied. The stress tensor was calculated with the stress theorem of Nielsen and Martin [19] and the C_{ijkl} with the generalized Hooke's law:

$$\sigma_{ij} - P\delta_{ij} = C_{ijkl}\epsilon_{kl}\,, \tag{1}$$

where σ_{ij} is the stress and ϵ_{kl} the strain. The bulk (K) and shear (μ) isotropic elastic moduli of aggregates were extracted from the elastic tensor, using the Voigt-Reuss-Hill averaging scheme [20]. Having the elastic coefficients, the acoustic wave velocities in each crystallographic direction could be calculated with the Christoffel equation:

$$[C_{ijkl}n_j n_l - \rho v^2 \delta_{ik}]p_k = 0\,, \tag{2}$$

where n_j is the versor in the j direction, ρ is the density, v is the velocity, and p_k is the wave polarization.

III. PROPERTIES OF $MgCO_3$

$MgCO_3$ may assume several crystalline forms, in which each magnesium atom has six nearest neighboring oxygen atoms and each carbon atom has three nearest neighboring oxygen atoms. At ambient conditions, it has a rhombohedral structure (magnesite), belonging to the $R\bar{3}c$ spacial group, which could be represented by a rhombohedral or a hexagonal lattice. The hexagonal lattice has a basis of 30 atoms and is more convenient for the analysis of experimental data, while the rhombohedral one has a basis of 10 atoms, being best suitable for theoretical investigations.

The material was simulated for pressures between −15 and 150 GPa, and the volume versus pressure results were fitted to a Birch-Murnaghan equation of state, shown in Fig. 1. Table I presents the structural parameters computed with both the LDA and GGA functionals, obtained out of the respective equations of state. According to the table, when compared to available experimental data [21], the LDA functional underestimates lattice parameters by about 1–2%, while the GGA one overestimates them by about 1–3%. It should be stressed that the theoretical values were obtained from static calculations, representing the condition of $T = 0$ K, except for the zero-point effect. On the other hand, experimental data were obtained at room temperature. The differences between theoretical and experimental lattice parameters are not associated with thermal effects, considering the small thermal expansion coefficients of magnesite ($\approx 15.9 \times 10^{-6}\,^{\circ}\mathrm{C}^{-1}$) [26]. However, considering that the LDA functional underestimates the lattice parameters, it appears to be a better model to describe this material as compared to the GGA one, since thermal effects would increase the LDA lattice parameters, getting closer to experimental values.

TABLE I. Structural properties of $MgCO_3$ ($R\bar{3}c$), $CaCO_3$ ($R\bar{3}c$), $MgCa(CO_3)_2$ ($R\bar{3}$), and $MgSiO_3$ (Pbnm) at $P = 0$. Lattice parameters (a, b, and c) are given in Å, volume (V_0) in Å^3, bulk moduli (K_0) in GPa, and bulk moduli derivative (K_0') are dimensionless.

		a	b	c	V_0	K_0	K_0'
$MgCO_3$	LDA	4.61		14.58	268.34	122	4.44
	GGA	4.70		15.20	290.77	100	4.48
	Expt.[a]	4.63		15.02	279.28	119	4.02
$CaCO_3$	LDA	4.96		16.53	352.45	72	3.65
	GGA	5.05		17.29	382.16	68	3.46
	Expt.[b]	4.99		17.07	368.11	73	4.00
$MgCa(CO_3)_2$	LDA	4.77		15.51	305.18	107	4.01
	GGA	4.87		16.21	332.59	86	4.08
	Expt.[b]	4.81		16.00	320.25	102	3.94
$MgSiO_3$	LDA	4.74	4.90	6.85	159.01	261	3.88
	GGA	4.83	4.98	6.98	168.13	231	3.93
	Expt.	4.78[c]	4.94[c]	6.91[c]	163.17[c]	264[d]	4.10

[a]Reference [21].
[b]References [22,23].
[c]Reference [24].
[d]Reference [25].

In terms of the bulk modulus, an inverse behavior was observed between the LDA and GGA results, when compared to experimental data. Again, the static results from the LDA functional provide a better comparison to room temperature experimental data, since thermal effects tend to soften the material, which would reduce the bulk modulus, getting LDA results closer to experimental values. All such trends and limitations of both LDA and GGA functionals are well documented in the literature for several other minerals [10]. Figure 1 shows that the LDA and GGA functionals, respectively, underestimate (≈3.9%) and overestimate (≈4.1%) the materials volume, within the pressure range used here, as compared to available experimental data [21].

High pressure experiments suggest that $MgCO_3$ is stable in the $R\bar{3}c$ phase up to 80 GPa [21,27]. Other experiments, based on x-ray diffraction, observed a transition to an unknown phase at pressures above 115 GPa and temperatures of 2100–2200 K [28], which is likely the $C2/m$ phase [12,13]. A theoretical investigation has identified a phase transition from $R\bar{3}c$ to $C2/m$ at 91 GPa [12]. Another recent theoretical investigation proposed that $MgCO_3$ is stable in the $R\bar{3}c$ phase for $P <$ 85 GPa, in the $P\bar{1}$ one between 85 and 101 GPa, and in the $C2/m$ one for pressures up to 140 GPa [13]. Other phases have

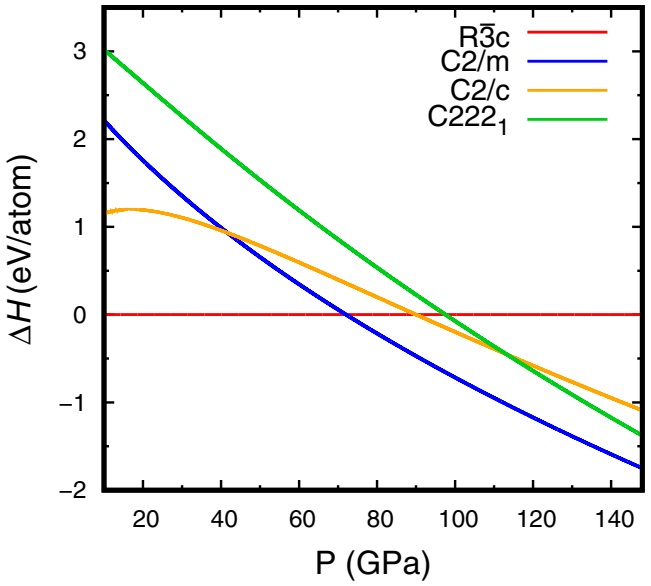

FIG. 2. Relative enthalpies (ΔH) of $MgCO_3$, computed with the LDA functional, for the $C2/m$ (blue line), $C2/c$ (orange line), and $C222_1$ (green line) phases, with respect to the $R\bar{3}c$ one (red line).

also been identified, but none of them has been found stable for pressures lower than 140 GPa [13], which is the pressure range of geophysical interest. The results of all those investigations agree that, at low pressures, $MgCO_3$ stays in the $R\bar{3}c$ phase and at higher pressures in the $C2/m$ one.

The $MgCO_3$ in the $C2/m$ phase has a basis with 30 atoms, in which the neighboring oxygen atoms form a tetrahedron around a carbon atom, while magnesium ones have coordinations of eight or ten. The relative stability of this phase, with respect to the $R\bar{3}c$, was here determined by the computation of the enthalpy of both phases at several pressures. Figure 2 shows the enthalpy of several $MgCO_3$ phases, as computed with the LDA functional. According to the figure, there is a phase transition at $P = 76$ GPa from the $R\bar{3}c$ to $C2/m$ phase, and the material stays in that phase at least up to 150 GPa. Calculations with GGA functional found the $R\bar{3}c$ to $C2/m$ transition at $P = 90$ GPa, in good agreement with available experimental [27,28] and theoretical [12] results. This investigation also explored two additional ($C2/c$ and $C222_1$) phases, which have been suggested in other investigations [29]. The results indicated that those two phases are not stable, for either LDA or GGA functionals, within the pressure range explored.

Figure 1 also shows the equations of state of the $C2/m$ phase as obtained with LDA and GGA functionals. Considering the results on enthalpy, shown in Fig. 2, in the pressure of the phase transition (76 GPa) there is a large crystal compression of about 6.6% with LDA and 6.5% with GGA. This pressure range is of great geophysical interest, especially because they correspond to depths near the middle of the lower mantle. If $MgCO_3$ is present, even in mild concentrations in the lower mantle, such large volume variation could impact the velocities of acoustic waves propagating across the mantle.

Determining the elasticity of the Earth's minerals is crucial to understand the properties of its interior, particularly in terms of its chemical composition and the propagation of seismic acoustic waves. We investigated the elasticity of $MgCO_3$, in the $R\bar{3}c$ and $C2/m$ phases, by computing the material elastic tensor with a set of deformations around the respective equilibrium configurations at pressures from 0 to 150 GPa. In the $R\bar{3}c$ phase, $MgCO_3$ belongs to the crystal class $\bar{3}m$ and, consequently, has six independent elastic constants. Table II presents the elastic constants of the material, obtained with the LDA functional, at null pressure in the $R\bar{3}c$ phase. When compared to experimental data, the results indicated that theoretical values are about 10% overestimated, consistent with trends observed for the bulk modulus. Such a comparison should take into account that the experimental data were obtained at room temperature, while theoretical calculations provided static values. Since increasing temperature, the trend is to soften the material and, therefore, reduces the strength of the elastic constants; a major part of this difference comes from thermal effects. If the high temperature behavior of the elastic coefficients and the bulk modulus are similar, it could be estimated that the theoretical elastic constants would reduce by about 5% at 300 K due to thermal effects, getting much closer to the respective experimental values. Such thermal effects on elastic constants were determined by computing the Gibbs free energy, with contributions of vibrations within the quasiharmonic approximation [36,37].

Table II presents the elastic constants of $MgCO_3$, in the $C2/m$ phase, obtained with the LDA functional. We observed that elastic constants in both ($R\bar{3}c$ and $C2/m$) phases increase almost linearly with increasing pressure, at least within the pressure range investigated here. Table II also presents the variation of the elastic constants for the $0 < \mathrm{P} < 150$ GPa range, with a linear fitting $C_{ij}(\mathrm{P}) = C_{ij}(0) + \alpha_{ij}\mathrm{P}$, where $\alpha_{ij} = \partial C_{ij}/\partial \mathrm{P}$.

The elastic constants of a material allow us to understand how it responds to external loads. On the other hand, from a geophysical point of view, the isotropic elastic constants determine how an isotropic mineral aggregate responds to an acoustic seismic wave. Those isotropic constants are generally computed with the Voigt-Reuss-Hill averages [20], using the computed elastic constants. Table II also presents those isotropic elastic constants for the $R\bar{3}c$ and $C2/m$ phases.

By comparing the independent elastic constants of $MgCO_3$ with the respective ones of $MgSiO_3$ in the perovskite structure ($Pbnm$), it is possible to observe that elastic constants of $MgCO_3$ are considerably smaller than those in $MgSiO_3$. Those results suggest that incorporation of carbon atoms in a $MgSiO_3$ matrix, in substitutional Si sites, softens the material, and could be a favorable process under high pressure conditions. Therefore, carbon incorporation in a $MgSiO_3$ aggregate should be energetically favorable in the lower mantle, and carbon could be dissociated within a $MgSiO_3$ matrix.

Figure 3 shows the acoustic wave velocities of $MgCO_3$ along several crystalline directions in the $R\bar{3}c$ and $C2/m$ phases, at the transition pressure ($P = 76$ GPa). According to the results, variations of the acoustic wave velocities for the two phases differ substantially, which indicates that there are major differences in their acoustic wave propagation, which may be quantified by the respective anisotropies. The anisotropy is obtained by the variations in the P and S acoustic wave velocities [38]. Figure 4(a) displays the anisotropy of $MgCO_3$ in the $R\bar{3}c$ and $C2/m$ phases. Overall, anisotropy is larger

TABLE II. Elastic constants (C_{ij}^{th}) and elastic moduli (K and μ) of $MgCO_3$ (in $R\bar{3}c$ and $C2/m$ phases), $CaCO_3$ (in $R\bar{3}c$, $Pmcn$, and $Pmmn$ phases), $MgCa(CO_3)_2$ (in $R\bar{3}$ phase), and $MgSiO_3$ (in $Pbnm$ phase) at $P = 0$ and their behavior with pressure, as computed with LDA functional. The table also presents the variation of elastic constants with pressure ($\alpha_{ij}^{th} = \partial C_{ij}^{th}/\partial P$) and available experimental values (C_{ij}^{exp}) for $MgCO_3$ (Ref. [30]), $CaCO_3$ (Refs. [31,32]), $MgCa(CO_3)_2$ (Refs. [33,34]), and $MgSiO_3$ (Ref. [35]). Elastic constants are given in GPa, and their derivatives are dimensionless.

	$MgSiO_3$ ($Pbnm$)			$MgCO_3$ ($R\bar{3}c$)			$MgCO_3$ ($C2/m$)		$CaCO_3$ ($R\bar{3}c$)			$CaCO_3$ ($Pmcn$)			$CaCO_3$ ($Pmmn$)		$MgCa(CO_3)_2$ ($R\bar{3}$)		
	C_{ij}^{th}	C_{ij}^{exp}	α_{ij}^{th}	C_{ij}^{th}	C_{ij}^{exp}	α_{ij}^{th}	C_{ij}^{th}	α_{ij}^{th}	C_{ij}^{th}	C_{ij}^{exp}	α_{ij}^{th}	C_{ij}^{th}	C_{ij}^{exp}	α_{ij}^{th}	C_{ij}^{th}	α_{ij}^{th}	C_{ij}^{th}	C_{ij}^{exp}	α_{ij}^{th}
C_{11}	479	482	3.651	283	261	5.380	343	4.815	177	148	6.558	210	171	7.964	120	6.141	228	205	5.298
C_{22}	544	537	5.555				418	4.963				134	110	7.125	283	6.946			
C_{33}	474	485	5.584	166	158	4.042	336	5.747	95	85	3.067	120	98	3.662	333	6.269	113	121	2.882
C_{44}	202	204	1.466	64	58	1.213	59	1.151	39	34	1.052	47	39	1.020	66	2.139	46	40	0.630
C_{55}	173	186	0.828				103	0.800				28	24	1.013	17	1.247			
C_{66}	156	147	1.625				122	1.157				49	40	2.199	13	0.530			
C_{12}	136	144	3.337	85	74	3.394	136	2.452	78	58	5.409	75	60	4.477	83	1.862	82	71	3.430
C_{13}	136	147	2.348	71	60	3.402	69	3.032	72	54	4.825	39	28	1.854	51	2.815	73	58	3.451
C_{14}				25	20	0.746			25	20	1.330						24	20	0.609
C_{15}							32	0.065									14	14	0.510
C_{23}	153	146	2.443				119	2.768				61	42	4.705	48	2.438			
C_{25}							39	0.388											
C_{35}							4	0.435											
C_{46}							2	0.402											
K	264	264	3.449	139	119	3.907	187	3.625	97	79	5.152	91	71	4.536	122	3.732	131	101	3.794
μ	181	177	1.383	89	78	1.218	98	1.384	40	43	0.939	43	37	1.484	56	1.787	62	59	0.879

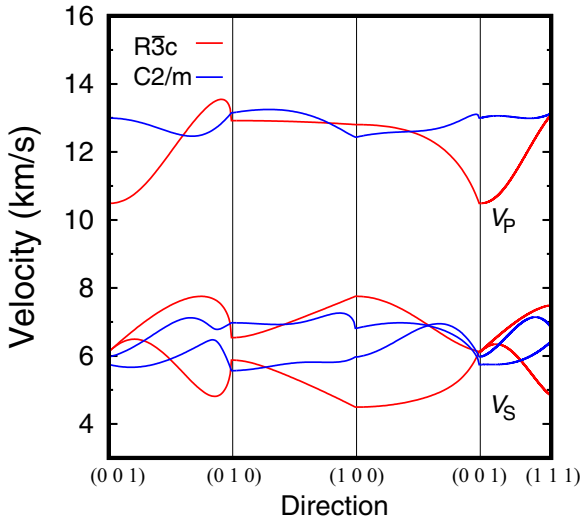

FIG. 3. Acoustic wave velocities of $MgCO_3$ in $R\bar{3}c$ (red lines) and $C2/m$ (blue lines) phases, along several crystalline directions, at the transition pressure $P = 76$ GPa.

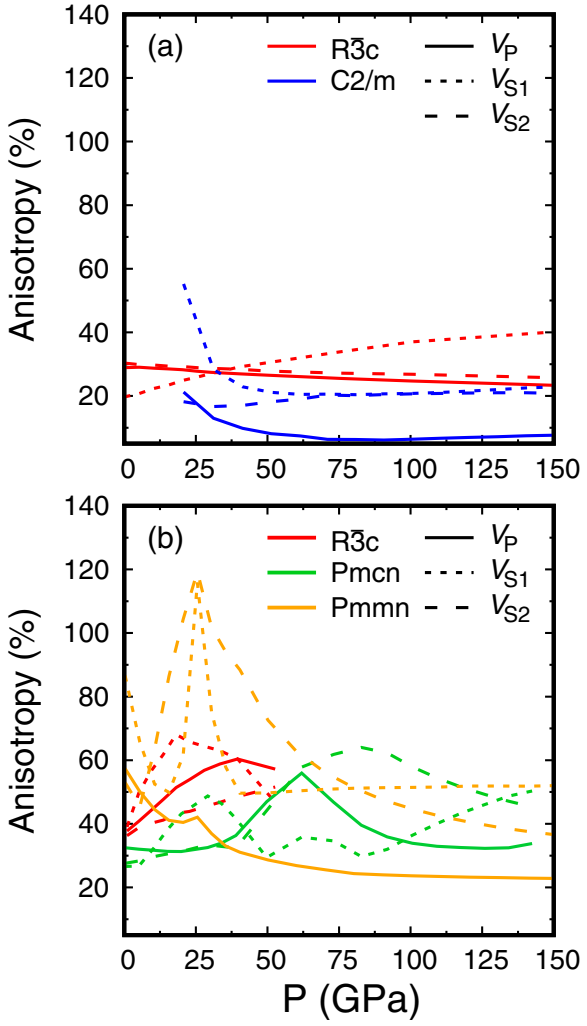

FIG. 4. Anisotropy of the acoustic wave velocities (V_P, V_{S1}, and V_{S2}): (a) $MgCO_3$ in the $R\bar{3}c$ (red lines) and $C2/m$ (blue lines) phases; (b) $CaCO_3$ in the $R\bar{3}c$ (red lines), $Pmcn$ (green lines), and $Pmmn$ (orange lines) phases.

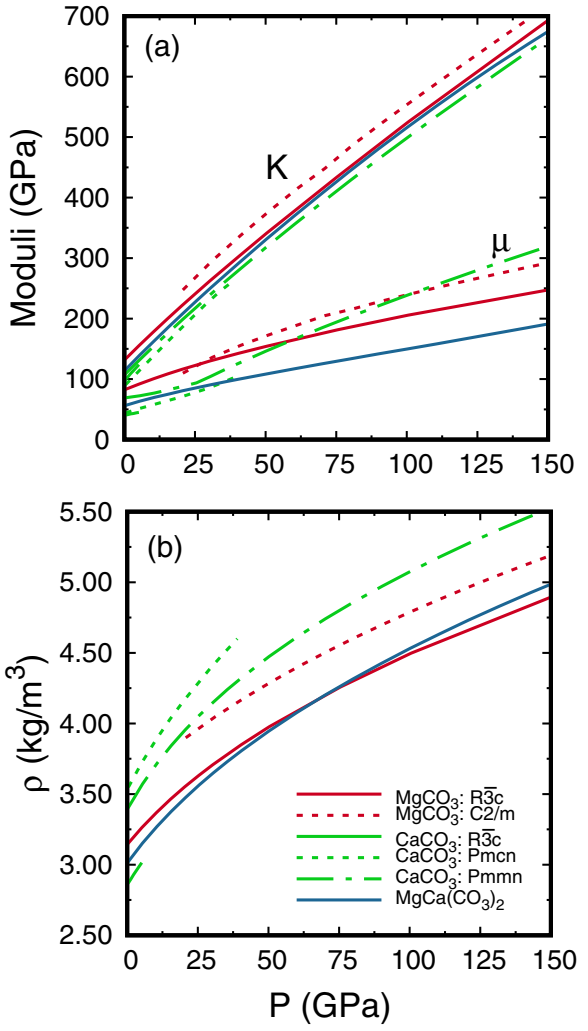

FIG. 5. (a) Isotropic elastic constants (K and μ) and (b) density (ρ) of $MgCO_3$ (red lines), $CaCO_3$ (green lines), and $MgCa(CO_3)_2$ (blue lines) in several stable phases.

in the $R\bar{3}c$ phase than in the $C2/m$ one. The anisotropy of $MgCO_3$ in those two phases are considerably different in the transition pressure ($P = 76$ GPa). Therefore, there is a major reduction in the overall anisotropy of the $MgCO_3$ as it follows such phase transition. Those results could have important geophysical implications [39].

Once having the isotropic elastic constants and densities at any pressure, shown in Fig. 5, it is possible to obtain the respective isotropic acoustic wave velocities. Figure 6 shows those velocities in $MgCO_3$ aggregates, in the pressure ranges of stability of the $R\bar{3}c$ and $C2/m$ phases. According to the figure, the isotropic wave velocities (V_P and V_S) increase with pressure. The figure also shows, as a reference, the respective isotropic wave velocities of $MgSiO_3$ aggregates, in perovskite ($Pbnm$) and post-perovskite ($Cmcm$) phases. The V_P and V_S acoustic wave velocities are considerably smaller in $MgCO_3$ than in $MgSiO_3$ at any pressure. Such behavior is a result of the smaller elastic constants of $MgCO_3$ as compared to those of $MgSiO_3$, despite also smaller densities. Particularly in the phase transition pressure of $MgCO_3$ ($P = 76$ GPa),

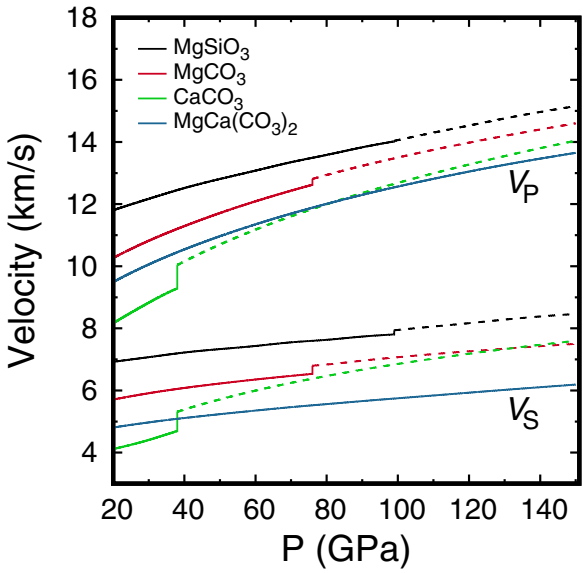

FIG. 6. Isotropic acoustic wave velocities (V_P and V_S) of $MgCO_3$ (red lines), $CaCO_3$ (green lines), and dolomite $MgCa(CO_3)_2$ (blue lines) aggregates. For reference, the wave velocities of $MgSiO_3$ aggregates (black lines) are also shown. The full and dashed lines represent the velocities for a mineral in its stable phase at each pressure. For $MgSiO_3$: $Pbnm$ (full lines) and $Cmcm$ (dashed lines) phases; for $MgCO_3$: $R\bar{3}c$ (full lines) to $C2/m$ (dashed lines), and for $CaCO_3$: $Pmcn$ (full lines) to $Pmmn$ (dashed lines).

there is a variation of 2.4% and 6.6% in the V_P and V_S acoustic velocities, respectively. Those small variations across the phase transition of $MgCO_3$ hamper an identification of such transition, by observing the acoustic waves in this mineral. In terms of geophysics, this transition may not be observed in the lower mantle. Considering the possible mild concentrations of $MgCO_3$, when compared to major mantle minerals $MgSiO_3$ and MgO, this change on wave velocities would be minimized. Additionally, there are several other important phenomena occurring in the lower mantle at the depths associated with this pressure range, such as the spin transition on those major mantle minerals [40].

A comparison of the isotropic acoustic wave velocities between $MgCO_3$ and $MgSiO_3$ aggregates at pressures over 100 GPa, presented in Fig. 6, may shed some light on the physical and chemical properties of the deep layers of the lower mantle. At those pressures, $MgCO_3$ is stable in the $C2/m$ phase while $MgSiO_3$ is either in the perovskite ($P < 100$ GPa) or post-perovskite ($P > 100$ GPa) phase [41]. It is well established in the literature that there are regions in the bottom of the lower mantle, close to the core mantle boundary, in which slow acoustic waves are observed [42]. Those regions, which have distinct properties, are labeled as ultra-low velocity zone (ULVZ), large low shear velocity provinces (LLSVP), or D″ [42,43]. The ULVZ is characterized by a major reduction on the S and P acoustic wave velocities. Several models have been proposed to explain the properties of those regions in the lower mantle, with suggestions of partial melting, high iron concentrations, iron partitioning, presence of water, and even another phase for the main mantle constituent $MgSiO_3$ (post-perovskite) [41,44]. The nature of those regions are considerably distinct, with different physical or chemical origins, and even different temperature profiles. Considering the profile of some of those low velocity zones, particularly their sharp boundaries, it is clear that only differences in thermodynamic properties could not explain their properties. Some chemical differentiation should be evoked to explain those properties [45].

In the light of our results, we explore the possibility that some of those low-velocity regions could be associated with the presence of carbonates near the core-mantle boundary. Those deep regions in the mantle are associated with pressures in the 100–130 GPa range. According to Fig. 6, for that pressure range, a $MgCO_3$ aggregate has seismic velocities considerably smaller than those of $MgSiO_3$, by more than 10% in the S waves and about 5% in the P waves. Therefore, those results suggest that $MgCO_3$ could be present in the deep lower mantle, and it could be the mineral responsible for the low velocities observed at those depths. Moreover, those results also provide an additional evidence that carbon could be stored in deep Earth as a carbonate mineral.

IV. PROPERTIES OF $CaCO_3$

Along with $MgSiO_3$ and MgO, $CaSiO_3$ is a major mineral in the Earth's lower mantle. However, the evidence of presence of carbon in the mantle raises the question on how it would be incorporated within those major minerals. While the previous section discussed the physical properties of $MgCO_3$, this section discusses the physical properties of $CaCO_3$, another mineral in which carbon could be incorporated in the lower mantle. This mineral has a structure that is considerably more complex than the one of $MgCO_3$, having several stable polymorphous for pressures in the range of the Earth's mantle.

Although $CaCO_3$ can be stabilized at the aragonite structure ($Pmcn$) at ambient conditions, calcite ($R\bar{3}c$) is the energetically favorable phase [13]. Calcite transforms into aragonite at 2.4 GPa and stays in this phase up to about 40 GPa, where there is a phase transition to the post-aragonite ($Pmmn$) structure. $CaCO_3$ has also other polymorphs, such as the vaterite structure.

Calcite belongs to the spacial group $R\bar{3}c$, similar to the magnesite structure, in which each calcium atom has six nearest neighboring oxygen atoms and each carbon atom has three nearest neighboring oxygen ones. Therefore, calcite is expected to have structural and elastic properties similar to magnesite, only taking into account the difference in their covalent radii ($R_{Mg} = 150$ pm and $R_{Ca} = 180$ pm). The equation of state of each $CaCO_3$ phase was established by searching for the equilibrium configuration for pressures ranging from −15 to 150 GPa, using both LDA and GGA functionals. Then, the structural parameters for null pressure were determined by fitting the results to a Birch-Murnaghan equation of state.

Table I presents the structural parameters of $CaCO_3$ in the $R\bar{3}c$ structure at equilibrium conditions ($P = 0$), obtained with LDA and GGA functionals. All structural parameters are within 3% from experimental data [22,23]. The lattice parameters of $CaCO_3$ are about 10% larger than those of $MgCO_3$, which is consistent with the larger covalent radius of Ca atoms as compared to Mg ones. In terms of the bulk

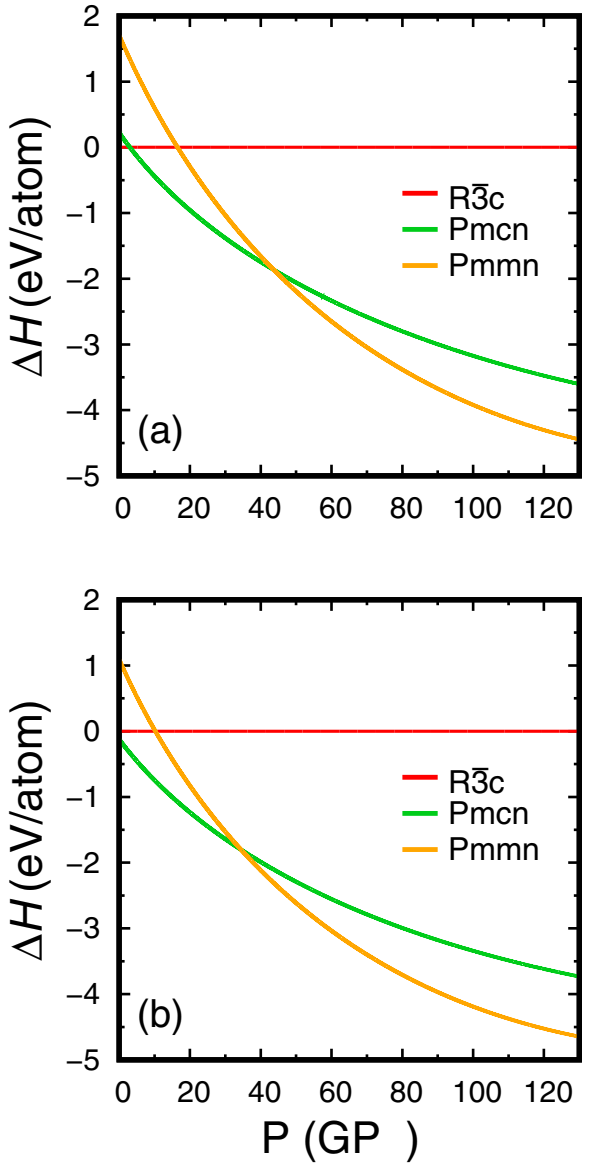

FIG. 7. Relative enthalpy (ΔH) of $CaCO_3$, computed with (a) LDA and (b) GGA functionals, for $Pmcn$ (red line) and $Pmmn$ (orange line) phases, with respect to $R\bar{3}c$ one (red line).

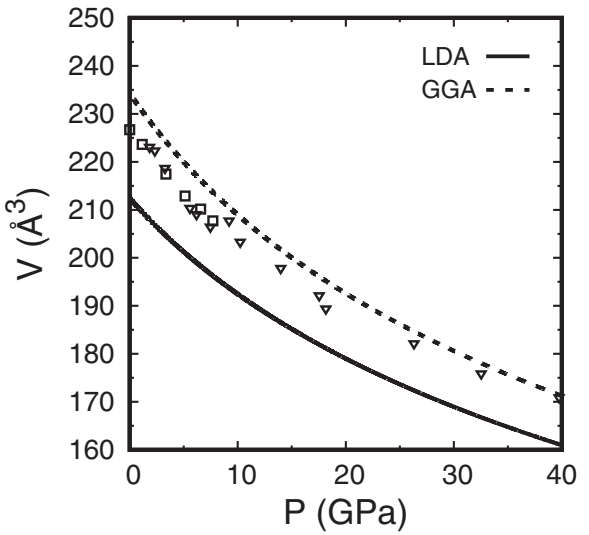

FIG. 8. Equation of state of $CaCO_3$ in the aragonite ($Pmcn$) phase, computed with the LDA (full lines) and GGA (dashed lines) functionals. Experimental data are from Refs. [48] (□) and [49] (▽).

modulus of the $R\bar{3}c$ phase, the LDA and GGA functionals give results in good agreement with the experimental value. According to the results, $CaCO_3$ is considerably softer than $MgCO_3$.

For high pressures, $CaCO_3$ may follow several structural phase transitions. Therefore, in order to explore the elastic properties of this mineral at high pressures, it is important to determine the stable structures at those pressures. Figure 7 shows the relative enthalpy of several $CaCO_3$ phases for pressures up to 150 GPa, as computed with LDA and GGA functionals. For the LDA functional, our results indicated that the aragonite ($Pmcn$) is already stable at $P = 0$. In fact, the LDA functional predicts a phase transition from calcite ($R\bar{3}c$) to aragonite ($Pmcn$) at $P = -2$ GPa, while experimental data indicates that this transition occurs at $P = 2.4$ GPa [46]. Additionally, this functional predicts a transition from aragonite ($Pmcn$) to post-aragonite ($Pmmn$) at $P = 38$ GPa, which is in good agreement with experimental results [47]. On the other hand, the GGA functional predicts those transitions, respectively, at 4 GPa and 40 GPa, also in good agreement with experimental data.

Figure 8 shows the equation of state of aragonite, compared to experimental results in the pressure range in which it is stable. The LDA functional underestimates the volume by about 6.0% and the GGA one overestimates it by about 3.0%. Although the GGA functional provides a better description on the structural properties and phase transition of $CaCO_3$, as compared to experimental data, the following paragraphs present its elastic properties using the LDA functional. This is motivated by the fact that the major focus is on the high pressure properties of $CaCO_3$, associated with those found in the Earth's lower mantle, in which the LDA functional provides consistent results in terms of phase stability. Furthermore, the results obtained with the LDA functional allow a better comparison with the elastic properties of $MgCO_3$, also computed with LDA functional, and presented in the previous section.

Table II presents the elastic constants of $CaCO_3$. In calcite phase ($R\bar{3}c$), $CaCO_3$ has six independent elastic constants, and in aragonite ($Pmcn$) phase it has an orthorhombic structure with nine independent elastic constants. As expected, the LDA functional overestimates all elastic constants, as compared to experimental values [31,32]. The table also presents the elastic constants of $CaCO_3$ in the post-aragonite ($Pmmn$) phase, indicating that the elastic constants of the post-aragonite phase are larger than those in the aragonite one.

Figure 4(b) shows the anisotropy of $CaCO_3$ in the $R\bar{3}c$, $Pmcn$, and $Pmmn$ phases. Clearly, there are considerable differences in anisotropy for those phases, particularly at low pressures. Additionally, the results indicate that $CaCO_3$ is more anisotropic than $MgCO_3$ in the pressure range investigated here.

Figure 5 shows the isotropic elastic constants of $CaCO_3$ aggregates in the $R\bar{3}c$, $Pmcn$, and $Pmmn$ phases, and Fig. 6 shows the respective isotropic acoustic wave velocities. The figure also shows, as a reference, the isotropic wave velocities of $MgSiO_3$ and $MgCO_3$ aggregates. First of all, in the $Pmcn$ to $Pmmn$ phase transition (at $P = 38$ GPa), there is a large increase in the V_P and V_S isotropic wave velocities of $CaCO_3$. Additionally, the wave velocities are considerably smaller in $CaCO_3$ than in $MgSiO_3$ and $MgCO_3$ aggregates, which results from its smaller elastic constants. Those results are particularly important for the region of about 100 to 120 GPa, which corresponds to the bottom of the lower mantle. The $CaCO_3$ aggregates, which would be stable in the post-aragonite phase ($Pmmn$) at those pressures, have acoustic wave velocities (V_P and V_S) that are much smaller than those of the major lower mantle constituent $MgSiO_3$. Therefore, the presence of $CaCO_3$ aggregates could also explain the existence of low velocity regions in the bottom of the lower mantle.

V. PROPERTIES OF $MgCa(CO_3)_2$

There is an additional carbonate phase that deserves attention from a perspective of minerals that could be present in the lower mantle. Since in $CaCO_3$ ($MgCO_3$) there are two types of Ca (Mg) sites, in the primitive cell, the replacement of a Ca (Mg) atom by a Mg (Ca) atom generates the dolomite, with the chemical symbol $MgCa(CO_3)_2$. It is well documented in the literature that dolomite decomposes in aragonite plus magnesite at high pressures [50,51]. By comparing the enthalpies of $MgCa(CO_3)_2$ in the dolomite phase with that of the mix of $CaCO_3$ in the magnesite phase plus $MgCO_3$ in the calcite phase, computed with the LDA functional, we found that $MgCa(CO_3)_2$ is stable only up to 40 GPa, decomposing into $CaCO_3$ plus $MgCO_3$ at higher pressures. Although at high pressures dolomite breaks up into aragonite plus magnesite [51–53], experimental studies have shown that these minerals should be stable at upper mantle conditions [50,51,53]. Therefore, it is still interesting to explore its physical properties.

Dolomite was simulated for pressures from −15 to 150 GPa, and the results were fitted to a Birch-Murnaghan equation of state. Dolomite has a rhombohedral crystalline structure and belongs to the $R\bar{3}$ spatial group, where each Ca or Mg atom has eight nearest neighboring oxygen atoms. Table I displays the results of the equation of state obtained with LDA and GGA functionals, which show trends equivalent to those presented by the other minerals. Comparing the results of the lattice parameters and bulk modulus of $MgCa(CO_3)_2$ with those of $CaCO_3$ and $MgCO_3$, they lie between the respective ones of magnesite and calcium carbonate minerals. In terms of elasticity, dolomite has seven independent elastic constants. Table II presents the theoretical elastic constants of dolomite, computed with the LDA functional, which are compared to experimental values [33,34]. Figures 5 and 6 show, respectively, isotropic elastic constants and isotropic acoustic wave velocities of dolomite. The wave velocities in this mineral are considerably smaller than those in the $MgSiO_3$ aggregates, at any pressure, remarkably for pressures up to 40 GPa.

VI. SUMMARY

In summary, we performed a first principles investigation on the structural and elastic properties of $MgCO_3$, $CaCO_3$, and $MgCa(CO_3)_2$ minerals at high pressures (up to 150 GPa), computed with LDA and GGA functionals. All the theoretical results for those minerals were in good agreement with available experimental data. The results allowed us to establish the elasticity of those minerals at high pressures. Particularly, the elastic constants allowed us to compute the isotropic acoustic wave velocities at high pressures. The results indicated that the S and P acoustic wave velocities in those carbonates are considerably smaller than the respective ones in $MgSiO_3$. Since $MgSiO_3$ is the main lower mantle constituent, these results indicated that the presence of regions rich in carbonates, either $MgCO_3$ or $CaCO_3$, in the lower mantle would cause a reduction on the acoustic wave velocities. This represents an additional model to explain the presence of several low-velocity zones in the lower mantle, observed near the core-mantle boundary. Those results also offer an additional model to explain where carbon could be stored in the deep mantle.

ACKNOWLEDGMENTS

This work was support by Brazilian agencies National Council for Scientific and Technological Development (CNPq), and São Paulo Research Foundation (FAPESP - Grant No. 2009/14082-3). M.L.M. thanks partial support from Coordenação de Aperfeiçoamento de Pessoal de Nível Superior (CAPES - Grant No. BEX 14456/13-3).

[1] A. R. Oganov, R. J. Hemley, R. M. Hazen, and A. P. Jones, Rev. Miner. Geochem. **75**, 47 (2013).

[2] A. S. Barnard, *The Diamond Formula: Diamond Synthesis: A Gemmological Perspective* (Butterworth-Heinemann, Linacre House, Jordan Hill, Oxford, 2000).

[3] R. M. Hazen and C. M. Schiffries, Rev. Miner. Geochem. **75**, 1 (2013).

[4] M. Javoy, Geophys. Res. Lett. **24**, 177 (1997).

[5] B. Marty and A. Jambon, Earth Planet. Sci. Lett. **83**, 16 (1987).

[6] B. Marty, C. M. O. Alexander, and S. N. Raymond, Rev. Miner. Geochem. **75**, 149 (2013).

[7] M. J. Walter, S. C. Kohn, D. Araujo, G. P. Bulanova, C. B. Smith, E. Gaillou, J. Wang, A. Steele, and S. B. Shirey, Science **334**, 54 (2011).

[8] M. C. Payne, M. P. Teter, D. C. Allan, T. A. Arias, and J. D. Joannopoulos, Rev. Mod. Phys. **64**, 1045 (1992).

[9] P. Giannozzi, S. Baroni, N. Bonini, M. Calandra, R. Car, C. Cavazzoni, D. Ceresoli, G. L. Chiarotti, M. Cococcioni, I. Dabo, A. Dal Corso, S. Fabris, G. Fratesi, S. de Gironcoli,

R. Gebauer, U. Gerstmann, C. Gougoussis, A. Kokalj, M. Lazzeri, L. Martin-Samos, N. Marzari, F. Mauri, R. Mazzarello, S. Paolini, A. Pasquarello, L. Paulatto, C. Sbraccia and S. Scandolo, G. Sclauzero, A. P. Seitsonen, A. Smogunov, P. Umari, and R. M. Wentzcovitch, J. Phys.: Condens. Matter **21**, 395502 (2009).

[10] B. B. Karki, L. Stixrude, and R. M. Wentzcovitch, Rev. Geophys. **39**, 507 (2001).

[11] A. R. Oganov, C. W. Glass, and S. Ono, Earth Planet. Sci. Lett. **241**, 95 (2006).

[12] A. R. Oganov, S. Ono, Y. Ma, C. W. Glass, and A. Garcia, Earth Planet. Sci. Lett. **273**, 38 (2008).

[13] C. J. Pickard and R. J. Needs, Phys. Rev. B **91**, 104101 (2015).

[14] W. Kohn and L. J. Sham, Phys. Rev. **140**, A1133 (1965).

[15] J. P. Perdew, K. Burke, and M. Ernzerhof, Phys. Rev. Lett. **77**, 3865 (1996).

[16] P. E. Blochl, Phys. Rev. B **50**, 17953 (1994).

[17] R. M. Wentzcovitch, Phys. Rev. B **44**, 2358 (1991).

[18] R. M. Wentzcovitch, J. L. Martins, and G. D. Price, Phys. Rev. Lett. **70**, 3947 (1993).

[19] O. H. Nielsen and R. M. Martin, Phys. Rev. B **32**, 3780 (1985).

[20] J.-P. Poirier, *Introduction to the Physics of the Earth's Interior*, 2nd ed. (Cambridge University Press, Cambridge, 2000).

[21] G. Fiquet and B. Reynard, Am. Mineral. **84**, 856 (1999).

[22] A. T. Simon, T. Redfern, and R. J. Angel, Contrib, Miner. Petrol. **134**, 102 (1999).

[23] H. Sitepu, Powder Diffr. **24**, 315 (2009).

[24] H. Horiuchi, E. Ito, and D. J. Weidner, Am. Mineral. **72**, 357 (1987).

[25] N. L. Ross and R. M. Hazen, Phys. Chem. Miner. **16**, 415 (1989).

[26] S. A. Markgraf and R. J. Reeder, Am. Mineral. **70**, 590 (1985).

[27] G. Fiquet, F. Guyot, M. Kunz, J. Matas, D. Andrault, and M. Hanfland, Am. Mineral. **87**, 1261 (2002).

[28] M. Isshiki, T. Irifune, K. Hirose, S. Ono, Y. Ohishi, T. Watanuki, E. Nishibori, and M. Takata, Nature (London) **427**, 60 (2004).

[29] W. R. Panero and J. E. Kabbes, Geophys. Res. Lett. **35**, L14307 (2008).

[30] J. Yang, Z. Mao, J. F. Lin, and V. B. Prakapenka, Earth Planet. Sci. Lett. **392**, 292 (2014).

[31] C. C. Chen, C. C. Lin, L. G. Lin, S. Sinogeikin, and J. D. Bass, Am. Mineral. **86**, 1525 (2001).

[32] L. Lin, C. Chen, and C. Lin, Phys. Chem. Miner. **32**, 97 (2005).

[33] P. Humbert and F. Plicque, C. R. Hebdom. Sean. Acad. Sci. Ser. B Paris **275**, 391 (1972).

[34] J. D. Bass, in *Mineral Physics & Crystallography: A Handbook of Physical Constants*, edited by T. J. Ahrens (American Geophysical Union, Washington, 1995), pp. 45–63.

[35] A. Yegaheh-Haeri, Phys. Earth Planet. Inter. **87**, 111 (1994).

[36] Z. Wu, J. F. Justo, C. R. S. da Silva, S. de Gironcoli, and R. M. Wentzcovitch, Phys. Rev. B **80**, 014409 (2009).

[37] Z. Wu, J. F. Justo, and R. M. Wentzcovitch, Phys. Rev. Lett. **110**, 228501 (2013).

[38] R. M. Wentzcovitch, B. B. Karki, S. Karato, and C. R. S. da Silva, Earth Planet. Sci. Lett. **164**, 371 (1998).

[39] S. L. A. Valcke, M. Casey, G. E. Lloyd, J. M. Kendall, and Q. J. Fisher, Geophys. J. Int. **166**, 652 (2006).

[40] R. M. Wentzcovitch, J. F. Justo, Z. Wu, C. R. S. da Silva, D. A. Yuen, and D. Kohlstedt, Proc. Natl. Acad. Sci. USA **106**, 8447 (2009).

[41] R. M. Wentzcovitch, B. B. Karki, M. Cococcioni, and S. de Gironcoli, Phys. Rev. Lett. **92**, 018501 (2004).

[42] S. Maruyama, M. Santosh, and D. Zhao, Gondwana Res. **11**, 7 (2006).

[43] A. K. McNamara, E. J. Garnero, and S. Rost, Earth Planet. Sci. Lett. **299**, 1 (2010).

[44] W. L. Mao, H.-K. Mao, W. Sturhahn, J. Zhao, V. B. Prakapenka, Y. Meng, J. Shu, Y. Fei, and R. J. Hemley, Science **312**, 564 (2006).

[45] J. P. Brodholt, G. Helffrich, and J. Trampert, Earth Planet. Sci. Lett. **262**, 429 (2007).

[46] G. J. F. MacDonald, Am. Mineral. **41**, 744 (1956).

[47] S. Ono, T. Kikegawa, Y. Ohishi, and J. Tsuchiya, Am. Mineral. **90**, 667 (2005).

[48] Y. Li, Y. Zou, T. Chen, X. Wang, X. Qi, H. Chen, J. Du, and B. Li, Am. Mineral. **100**, 2323 (2015).

[49] J. Vizgirda and T. J. Ahrens, J. Geophys. Res. **87**, 4747 (1982).

[50] C. Biellmann, P. Guyot, J. Peyronneau, and B. Reynard, Earth Planet. Sci. Lett. **118**, 31 (1993).

[51] A. Buob, R. W. Schmidt, and P. Ulmer, Am. Mineral. **91**, 435 (2006).

[52] I. Martinez, J. Zhang, and R. J. Reeder, Am. Mineral. **81**, 611 (1996).

[53] Y. Zhu and Y. Ogasawara, Geology **30**, 947 (2002).